4D Printing of Multifunctional Devices Induced by Synergistic Role of Magnetite and Silver Nanoparticles in Polymeric Nanocomposites

ADVANCED FUNCTIONAL MATERIALS
www.afm-journal.de

4D Printing of Multifunctional Devices Induced by Synergistic Role of Magnetite and Silver Nanoparticles in Polymeric Nanocomposites

Andrea Cosola, Ignazio Roppolo, Francesca Frascella, Lucia Napione, Gabriele Barrera, Paola Tiberto, Florian Turbant, Veronique Arluison, Isabelle Caldelari, Noémie Mercier, Micaela Castellino, Florian Aubrit, and Giancarlo Rizza*

Emerging as a revolutionary strategy to fabricate dynamic three dimesional (3D) structures, 4D printing (4DP) mainly refers to printed materials capable of changing form over time when exposed to a predetermined stimulus. Nevertheless, the 4D concept can be extended beyond shape-morphing, by including also changes in the properties and/or functionalities of printed materials over time. To this end, this work explores the 4DP of multifunctional nanocomposites that can adapt to different application scenarios exploiting the stimuli-activable properties of two functional nanofillers embedded into the polymeric matrix. In particular, a photocurable system loaded with both Fe_3O_4 nanoparticles (NPs) and $AgNO_3$, as precursors for the in situ photo-induced generation of Ag NPs, is used for the digital light processing of magnetic nanocomposites with integrated electrical and antibacterial functions. The composition of formulations is designed to both optimize their printability and maximize the magneto-responsiveness and the electrical conductivity and/or antibacterial activity of the printed objects, given by Fe_3O_4 and Ag NPs, respectively. Finally, it is shown that the functional responses of the nanocomposites can be activated individually or in combination, which may be of particular interest for the fabrication of smart multifunctional devices with potential applications ranging from soft electronics to biomedicine.

1. Introduction

Materials science is based on the three-way relationship between material properties, fabrication methods, and design. For a long time, however, their synergistic interaction has been limited by the inherent challenges of managing all those three parameters at the same time. However, in the last 30 years, the development of 3D printing (3DP) technology allowed for the fabrication of customizable 3D architectures using Computer Aided Design (CAD) software, deeply exploiting thus the relationship between fabrication and design.[1,2] Due to its almost limitless design freedom, rapid and affordable manufacturing, and the ability to print a wide range of materials, 3DP has attracted considerable interest in both academia and industry and paved the way for groundbreaking advances in fields ranging from aerospace to medicine.[3–5] On the other hand, because the most common use of 3DP was for

A. Cosola, I. Roppolo, F. Frascella, L. Napione, M. Castellino
Department of Applied Science and Technology
Politecnico di Torino
Corso Duca degli Abruzzi 24, Torino 10129, Italy
E-mail: ignazio.roppolo@polito.it

A. Cosola, F. Aubrit, G. Rizza
Laboratoire des Solides Irradiés (LSI)
CEA/DRF/IRAMIS
Ecole Polytechnique
Centre National de la Recherche Scientifique UMR7642
Institut Polytechnique de Paris
Palaiseau 91128, France

The ORCID identification number(s) for the author(s) of this article can be found under https://doi.org/10.1002/adfm.202406226

DOI: 10.1002/adfm.202406226

I. Roppolo, F. Frascella, L. Napione
PoliTOBioMEDLab
Politecnico di Torino
Corso Duca degli Abruzzi 24, Torino 10129, Italy

G. Barrera, P. Tiberto
Advanced Materials for Metrology and Life Sciences Division
INRiM
Strada delle Cacce 91, Torino 10143, Italy

F. Turbant, V. Arluison
Laboratoire Léon Brillouin
Centre National de la Recherche Scientifique
Université Paris Saclay
Gif-sur-Yvette 91190, France

F. Turbant
Synchrotron SOLEIL
L'Orme des Merisiers
Saint Aubin BP48, Gif-sur-Yvette 91192, France

V. Arluison
Université Paris Cité
UFR SDV
Paris 75013, France

prototyping studies and the fabrication of static elements, the role of materials properties remained for a long time underrated.[6] The possibility to synergistically take advantage of the above-mentioned threefold relationship occurred when Prof. Skylar Tibbits introduced smart materials into the 3DP processes.[7] Historically, the creation of smart materials, also known as active or programmable matter, is due to the initiatives in materials development, spearheaded by the Defense Advanced Research Projects Agency (DARPA).[8,9] The most widespread definition of smart materials consists of materials able to respond to external stimuli actively modifying their properties, enabling dynamic adaptation to surrounding conditions. Among them, it is worthy to mention shape memory, photo-active, piezo-electric, and magnetorheological materials.[10–12]

In his 2014 publication, Prof. Tibbits referred to 4D printing (4DP) as "one recent example of Programmable Matter" and introduced a 4th dimension, time, into this new additive manufacturing strategy.[13,14] While Tibbits' definition emphasizes material composition and manufacturing processes, it leaves room to describe the interaction between the printed component and applied stimuli. Specifically, he emphasizes the importance of a design process that takes into account the geometric, physical, and mechanical properties of materials, as well as their dynamic responses to specific external stimuli over time. This explains the reason why the term "4D printing" predominantly refers to systems capable of undergoing shape changes.[15,16] However, there is a semantic difference between time and function (or propriety). Indeed, smart materials possess intrinsic functions that are activated by external stimuli, and these functions remain active during the application of these stimuli. Otherwise stated, time is related to the duration rather than to the cause of the induced phenomenon.

Defining 4DP in terms of functions (or material's properties) rather than time allows thus for a widening of the concept, by integrating other phenomena than shape changes. Besides, the search for functionality may unlock unforeseen possibilities, reshaping 3DP processes, introducing adaptability and autonomy capabilities in engineered objects, and giving, among others, further input to the development of 4DP, that makes the use of materials with stimuli-adaptable functions its core principle.

In this regard, two strategies are being developed to achieve multifunctionality through 3DP. The first one focuses on "macroscopic" multi-material printing, where achieving the desired shape or property changes involves the complexity of heterogeneous printing, i.e., the synergistic or complementary interaction between printable materials, whether in the form of solid filaments or viscous resins.[17–19] The goal is to assign suitable materials, in the form of passive or active elements, layers, or voxels, to specific locations within the construct. This ensures that the printed components possess the appropriate spatial and temporal stimuli and/or actuator characteristics.[17,19–21]

I. Caldelari, N. Mercier
Université de Strasbourg
CNRS
Architecture et Réactivité de l'ARN
UPR9002, Strasbourg F-67000, France

The second approach focuses on the integration of micro- and nano-structures within printed constructs, thus expanding the scope of nanotechnologies in the field of additive manufacturing.[22–24] Indeed, beyond their conventional use as reinforcing agents, micro- and nanomaterials can also provide extra functionalities to the printed components, serving, for instance, as conductive,[25–31] optical,[32] piezoelectric;[33] sensing,[34,35] bioactive,[36] acoustic,[37] magnetic,[38–42] or photothermal elements.[43–45]

Following this second approach, in this manuscript, we extend the concept of multifunctionality by incorporating into a photocurable resin two types of nanofillers, each with specific functions that can be exploited individually or synergistically. This represents a further step in the development of 3D printed devices, overcoming the concept of "simple" functionality, toward the idea of multifunctionality. For instance, the integration of soft magnetic magnetite nanofillers into printable matrix is attracting extensive research interest. Indeed, due to their ability to undergo fast and reversible actuation or locomotion, or even programmable shape changes under the application of magnetic fields, magnetic nanocomposites are showcasing significant potential in many practical applications, including soft robotics,[39,46–49] soft electronics,[50] and numerous biological applications.[51] Conversely, silver nanoparticles were largely investigated in 3DP for their well-known conductive,[52,53] antimicrobial[54] and plasmonic properties.[55] The core of our approach is to utilize these properties either independently or synergistically. For example, one can leverage the magnetic properties for soft robotics and the conductive properties for electrical transport individually or combine them to create magneto-electric systems. Likewise, one can imagine designing magnetically-driven devices to locally exhibit antibacterial activity.

In this context, this study aims to develop a novel class of Digital Light Processing (DLP)-printable nanocomposites displaying simultaneously magneto-responsiveness, enabled by Fe_3O_4 NPs, and electrical conductivity and/or antibacterial activity, given by Ag NPs. However, this seek is not priceless, and the presence of NPs may modify resin stability, viscosity, the kinetics of photopolymerization, and ultimately printability.[56,57] Consequently, the design of the printable formulation is of paramount importance to gather all these aspects.

To this end, expanding findings of previous research, in this study, a photocurable poly(ethylene glycol) diacrylate (PEGDA) oligomer was loaded with magnetite nanoparticles (Fe_3O_4 NPs),[58–60] and silver nitrate ($AgNO_3$), used as a precursor for the postprinting photogeneration of silver nanoparticles (Ag NPs).[61,62]

Referring to the peculiar challenges of vat polymerization, light-induced 3DP of magnetic nanocomposites requires careful optimization of the printable formulations.[63–65] Moreover, the incorporation of silver into the polymeric matrix via the in situ reduction of silver precursors through postprinting thermal, electrochemical, or photochemical approaches,[66–69] is preferable to the direct dispersion of Ag NPs.[70–72] Indeed, the former strategy allows an easy and effective controlled generation of the nanofiller, without affecting the viscosity of the photocurable resins, and avoids problems of sedimentation or of decrease of the kinetics of polymerization, hence maintaining high printability.[61,62,73,74]

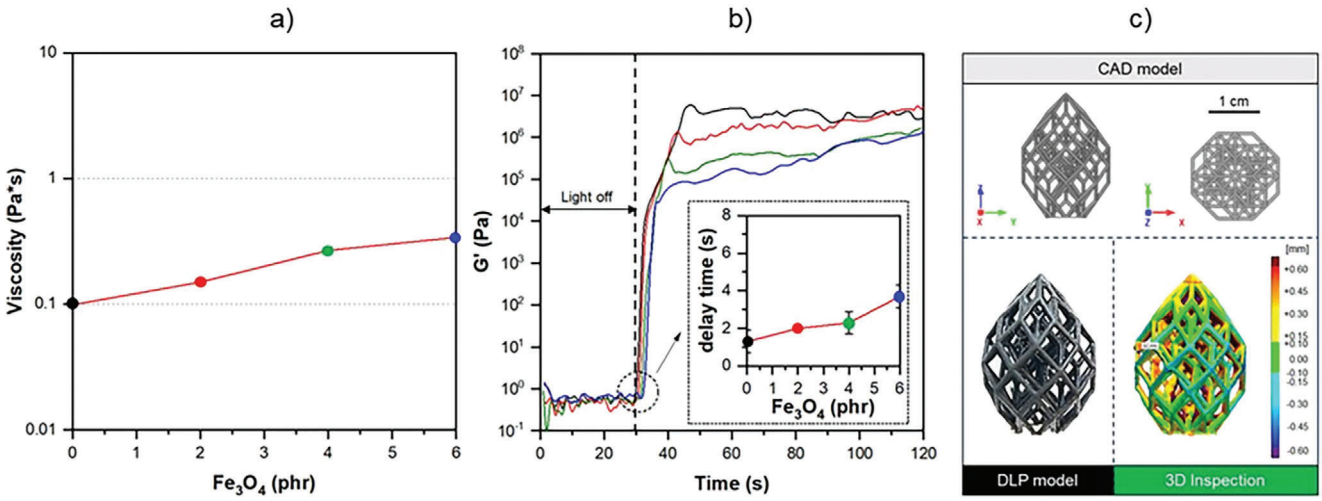

Figure 1. a) Influence of increasing Fe_3O_4 content on the formulation viscosity; b) photoreology curves corresponding to the evolution of the storage modulus (G') of the photocurable formulations with inset graph giving the delay on the onset of photopolymerization as a function of the Fe_3O_4 content; c) diamond-shaped 3D-structure DLP-printed from the photocurable formulations containing the maximum amount of Fe_3O_4 NPs (6 phr), and heat-map obtained by 3D scanning representing the fidelity of the printed structure to the corresponding digital CAD model.

Based on the previous considerations, the composition of the photocurable formulations was carefully designed to optimize their DLP printability while maximizing the functional response of the printed materials. Finally, as a proof of concept, we show that the different functional responses can be activated individually or in combination, such as for creating remotely controllable magnetic 4D structures, electrically conductive devices, antibacterial features, and magneto-electric controllable elements, with potential applications ranging from soft electronics to biomedicine.

2. Result

2.1. Design, Characterization, and Printability of the Photocurable System

Multifunctional magnetic nanocomposites with integrated electrical and antibacterial properties were fabricated by exposing a photocurable oligomer (polyethylene glycol diacrylate, PEGDA) embedding iron oxide nanoparticles (Fe_3O_4 NPs) and silver nitrate ($AgNO_3$), first to a DLP apparatus, and then to a UV-radiation in the presence of a two-components radical photogenerating-system.

In particular, because the DLP machine works with a light source emitting in the visible range, a photoinitiator working in the near UV-violet-blue, phenylbis(2,4,6-trimethylbenzoyl)phosphine oxide (BAPO), was chosen. In contrast, a second photoactive compound absorbing in the deeper UV, 2-hydroxy-2-methyl-1-phenyl-propan-1-one (HMP), was employed to exploit the typical UV postprinting process to support the *in-situ* photoreduction of silver cations (Ag^+) into silver nanoparticles (Ag NPs).[62]

Based on previous studies,[58–60] preliminary investigations were conducted to evaluate the effect of the addition of Fe_3O_4 NPs on the viscosity, stability, and photoreactivity of the formulations, aimed to assess their DLP printability. To this end, a first set of formulations was prepared by dispersing in PEGDA increasing amounts of Fe_3O_4 NPs, while the content of $AgNO_3$ was initially kept constant (5 phr).

As shown in **Figure 1**a, rheology measurements evidenced that the viscosity (η) of the formulations was not affected by increasing the content of Fe_3O_4 NPs up to 6 phr, with η values (0.1–0.35 Pa s^{-1}) remaining in the typical range reported for DLP printable resins (0.001–1 Pa s^{-1}).[75–77] This behavior, as already reported, can be ascribed to the lubricant effect of the spherical-shaped nanofiller.[58] Moreover, neither sedimentation nor agglomeration was observed in the formulations for at least 2 h, regardless of the content of Fe_3O_4 NPs (see results of the settlement stability tests in Figure S1, Supporting Information). This is generally compatible with the printing times to obtain a homogeneous magnetic response in the printed parts.[58]

In contrast, real-time photorheology tests performed during visible light irradiation showed that the addition of Fe_3O_4 NPs slightly affected the reactivity of the formulations. In particular, increasing amount of nanofiller caused an ever-increasing delay on the onset of photopolymerization (i.e., the time needed to observe the increase of the storage modulus G' after switching on the light, Figure 1b), which suggests the need of longer exposure time during printing, although it is important to stress that the best printing parameters are always empirically defined, on the basis of the printing accuracy.[78,79]

This phenomenon can be ascribed to a competitive absorption between the photoinitiator (BAPO) and the nanofiller (absorption coefficient of Fe_3O_4 in the visible range of $\approx 2 \times 10^5$ cm^{-1}),[58,80] which leads to a decrease of the quantum yields of initiation[81] of the former and then to the slowing down of the photopolymerization kinetics.

Hence, optimizing the printing parameters, that is setting longer exposure for increasing content of Fe_3O_4 NPs, enabled the fabrication of highly complex 3D lattice structures (Figure 1c; Figure S2, Supporting Information) with high fidelity to the original CAD models (average deviation between positive and

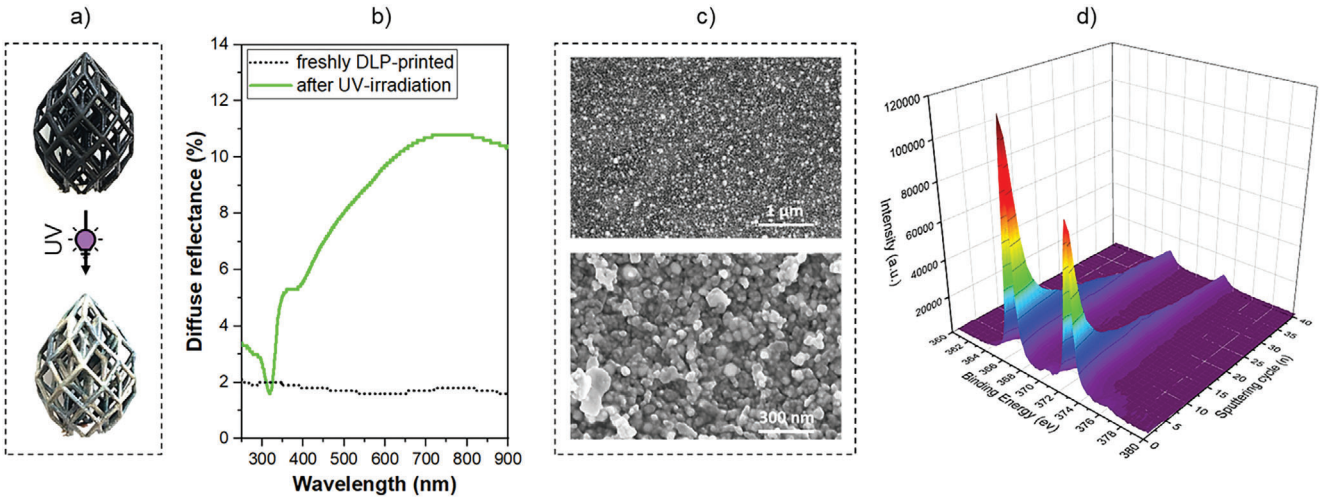

Figure 2. a) Example of a 3D object and its irreversible color change from black to silver-mirror-like related to the photo-induced generation of Ag NPs during the UV postprinting process (10 min, 100 mW cm^{-2}); b) diffuse reflectance spectra of a DLP printed nanocomposite before and after the postprinting UV-irradiation; c) FESEM images of the nanocomposite sample $NC_{6;5*}$ after the UV postprocessing; d) XPS depth profile accumulation curves of Ag atoms for the nanocomposite sample $NC_{6;5*}$.

negative displacements of the DLP printed diamond-shaped part of Figure 1c from its digital model was found to be ≈+0.082 mm). Noteworthy, Fe_3O_4 NPs contents higher than 6 phr have not been considered in this work because it was already reported that over this amount 3D printing process results were affected, leading to further decrease of polymerization kinetics due to a competition between the photoinitiator and the nanofiller in absorbing light radiation, as well as decreased printing accuracy and poor mechanical performance of the printed parts.[58] For the sake of clarity, henceforth DLP-printed nanocomposites will be referred to as $NC_{x;y}$, where x and y are the concentrations of Fe_3O_4 and $AgNO_3$ loaded in the photocurable formulations in phr, respectively.

2.2. Postprinting Photo-Generation of Ag NPs

The printed samples were then submitted to a UV-postprocessing to induce the in situ reduction of Ag salts and the formation of Ag NPs. Indeed, it is known that when exposed to UV irradiation in the presence of an electron donor compound, such as the hydroxyketone used in this work (HMP), silver cations (Ag^+) undergo reduction to form silver metal atoms (Ag^0). These, in turn, act as nucleation centers of Ag NPs.[82,83] As previously mentioned, referring to vat polymerization, postprinting in situ reduction of silver precursors is preferable to the direct dispersion of Ag NPs,[70–72] since it avoids: i) increased viscosity of the formulations, which can lead to flow problems during 3D printing and reduced mobility of growing macroradicals; ii) sedimentation or agglomeration of the nanofiller; and iii) decreased polymerization kinetics of the photocurable resin, as Ag NPs can scatter/absorb light, competing with the photoinitiator and consequently reducing the photopolymerization rate and depth of light penetration.[61,62,73,74]

Macroscopically, an irreversible color change from black to a silver-mirror-like appearance (**Figure 2a**) was observed when exposing the $NC_{x;5}$ nanocomposites to a long UV-irradiation (10 min, 100 mW cm^{-2}). This optical effect, typically related to the surface plasmon resonance of Ag NPs distributed within a polymeric matrix,[62,84,85] suggests the generation of silver-rich surfaces containing a high density of Ag NPs.

This finding is supported by UV–vis spectroscopy measurements. As shown in Figure 2b, no significant reflectance was observed for the freshly printed samples $NC_{x;5}$, confirming that no silver reduction occurred during the visible-light irradiation performed with the DLP machine, in good agreement with what was already reported.[62] In contrast, a significant increase in the visible-to-infrared reflectance was observed in the spectrum of the samples subjected to UV-postprocessing (henceforth referred to as $NC_{x;y}$*), with two well-defined dips appearing at ≈320 and 390 nm, which can be typically observed in the diffuse reflectance spectra of thin nanocrystalline silver films.[86] The dip at a lower wavelength is attributed to the bulk plasma frequency of Ag, as the result of the d-like valence electron absorption. while the second one is generally associated with the surface plasmon resonance of Ag NPs (Figure 2b), although slightly blue-shifted from the classic ≈400 nm peak.[9,86]

Field emission scanning electron microscopy (FESEM) images further confirmed the generation of silver-rich surfaces with a dense distribution of generally spherical-shaped Ag NPs (Figure 2c), with sizes up to 150 nm. X-ray photoelectron spectroscopy (XPS) depth-profile analyses revealed a surface enrichment of Ag NPs, in agreement with FESEM results, with a gradient distribution within the polymeric matrix.

High resolution (HR) spectra of the Ag core peaks region produced during 40 cycles of depth-profiling analysis on the $NC_{6;5}$* nanocomposites are reported, as a way of example, in Figure 2d. Note that the sample containing 6 wt.% of Fe_3O_4 NPs (shown in Figure 2a–c) is representative of all the $NC_{x;5}$* composites loaded with different Fe_3O_4 NPs concentrations.

As clearly evident from the cascading spectra, the intensity of the doublets corresponding to the binding energies of silver

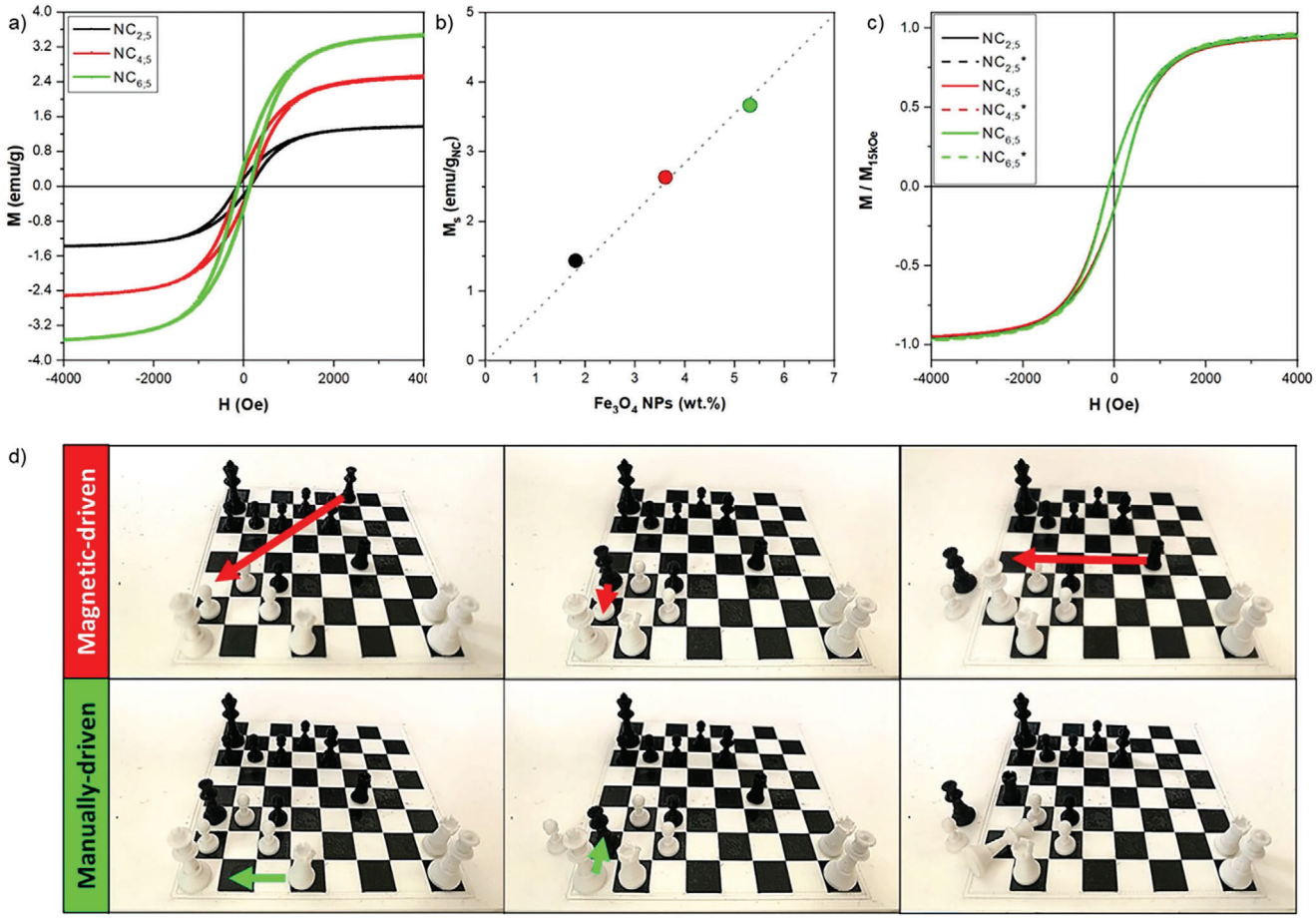

Figure 3. a) Room temperature hysteresis loops and b) evolution of saturation magnetization values for the freshly printed nanocomposites $NC_{x;5}$ as a function of the content of Fe_3O_4 NPs; c) normalized hysteresis loops measured on the $NC_{x;5}$ and $NC_{x;5}$* samples for selected Fe_3O_4 NPs content; d) example of the magnetically-triggered control of the translation of a DLP printed chess loaded with 6 phr of Fe_3O_4 NPs: the white checkers are moved by hand, while the black ones, i.e., the magneto-responsive ones, are moved by a localized magnetic field generated below the chessboard.

atoms in their zero-valent state (Ag $3d_{5/2}$ and $3d_{3/2}$ doublets at 368.24 and 374.24 eV,[84,87] (see Ag3d HR spectrum in Figure S3, Supporting Information for details) starts to decrease after ≈10 cycles, confirming that Ag NPs tend to accumulate in the first layers of the UV postirradiated nanocomposites. It must be noted also that XPS, in good agreement with previous results, didn't show the presence of unreacted silver ions.[61,62,73,84,85,88] As already reported, this accumulation effect can be ascribed to two different phenomena, namely the light penetration depth and the diffusion processes driven by formation–growth–destruction and rebuilding mechanisms. On the one hand, the nucleation and growth of the Ag NPs preferably occur on the surface closer to the light source, i.e., where the higher number of photogenerated radicals induce the photoexcitation and reduction of a higher number of silver cations. On the other hand, a temperature gradient induced by light exposure could be the driving force for a time-dependent accumulation of Ag clusters on the irradiated sample surface due to classical diffusivity laws.[85]

As a support of this hypothesis, the low glass transition temperature of the polymeric matrix (T_g ≈ −30 °C), may enable an extended diffusivity and migration of Ag species toward the nanocomposite surfaces during the UV-light exposure because of a high-temperature gradient ($T > T_g$).[84] Finally, the step-by-step formation of a NPs-rich surface further prevents light penetration, due to enhanced reflectivity.

2.3. Magnetic Properties of the Multifunctional Fe_3O_4-Ag Nanocomposites

Room-temperature hysteresis loops were measured to evaluate the magnetic behavior of the DLP-printed nanocomposites. The M(H) curves exhibited a similar magnetization reversal process characterized by a hysteretic behavior (**Figure 3a**), with a coercive field (Hc) of ≈130 Oe, regardless of the content of Fe_3O_4 NPs. The Hc value is compatible with Fe_3O_4 NPs of 50–100 nm diameter in a multidomain state.[58] The saturation magnetization (Ms) of the nanocomposites, calculated by normalizing the magnetic moment recorded at H = 15 kOe to the sample mass, increases linearly as the amount of Fe_3O_4 NPs loaded in the polymer matrix (Figure 3b). Noteworthy, the precipitation of Ag NPs does not affect the magnetic response of the nanocomposites, as confirmed by the perfect overlap of the normalized hysteresis loops

measured on the $NC_{x;5}$ and $NC_{x;5}$* samples, regardless of the content Fe_3O_4 NPs content (Figure 3c). This is consistent with the diamagnetic character of Ag, which provides a negligible magnetic signal compared to the ferrimagnetic one of Fe_3O_4.

As proof of concept, a set of samples loaded with increasing content of Fe_3O_4 NPs were then printed and subjected to an external magnetic field, to prove the possibility to remotely control their motion. An example of the magnetically-triggered control of the translation of a DLP-printed chess loaded with 6 phr of Fe_3O_4 NPs is given in Figure 3c and Movie S1 (Supporting Information), which show a chess game where the white checkers are moved by hand, while the black ones, i.e., the magneto-responsive ones, are moved by a localized magnetic field. As expected, the results evidenced that increasing the amount of the magnetic nanofiller inside the nanocomposite objects allows for lowering the magnetic field required to enable their response, since the magnetic force is proportional to the product of the magnetization of the object, its volume, and the field gradient.

Pursuing the goal of designing a 4D printable multifunctional material, the possibility of exploiting the photogenerated Ag NPs to impart to the magnetic nanocomposite two additional functionalities, i.e., electrical and antibacterial, was explored. Indeed, Ag NPs have attracted extensive research interest as microelectronic[89] and antibacterial materials[90,91] because of their superior physiochemical properties.

Thus, a new set of formulations was synthesized and printed varying the amount of $AgNO_3$, while the Fe_3O_4 NPs content was kept fixed at 6 phr to maximize the magnetic response of the nanocomposites, as discussed above.

In this case, the goal was to assess how the content of Ag NPs in the polymeric matrix influences the electrical conductivity and antibacterial activity of the nanocomposites.

2.4. Electric Behavior of the Multifunctional Fe_3O_4-Ag Nanocomposites

First, electrical measurements were performed to evaluate the resistance decrease related to the photogeneration of Ag NPs. The results showed that all the postprinting UV-irradiated $NC_{6;y}$* samples behave as Ohmic materials (Figure S4, Supporting Information) and their resistance decreases when increasing the content of $AgNO_3$ up to 10 phr (see semilogarithmic I/V plot given in **Figure 4a**). In particular, the surface resistivity (ρ_s) decreases by two orders of magnitude in the presence of 2.5 phr of $AgNO_3$, and then further decreases by almost another order of magnitude when increasing the content of Ag NPs precursor up to 5 phr. This can be related to higher surface-enrichment of Ag NPs which allows charge transfer (see Figure 4b), in good agreement with XPS and EDX measurements. In contrast, no significant decrease in resistivity was observed by increasing the $AgNO_3$ content to 10 phr. This is consistent with the generation of a percolative path among Ag NPs, as confirmed by FESEM images (see Figure S5, Supporting Information). Consequently, the total resistance is determined by inter-NPs dissipation mechanisms.[62,92] In this context, it should be mentioned that a further amount of $AgNO_3$ wasn't added as this implied solubility problems without conductivity benefits.

The values of resistivity measured are typical for dissipative materials and, in the case of magneto-responsive nanocomposite doped with 10 phr of $AgNO_3$, they were sufficient to achieve the illumination of an LED circuit when using our material as a resistive component of an electrical circuit (Figure 4c; Movie S2, Supporting Information).

Finally, the possibility to design a multifunctional device capable of performing multiple tasks by responding selectively to magnetic and electric stimuli was explored. Hence, a magneto-electric object was first DLP printed from a precursor formulation loaded with the maximum content of Fe_3O_4 NPs and $AgNO_3$ being investigated in this study (6 and 10 phr, respectively) and then UV-irradiated, to induce the photogeneration of Ag NPs. Subsequently, as proof of concept, it was forced to move by the application of an external magnetic field (H = 50 mT) into a labyrinth containing three open electric circuits. As shown in Figure 3d and Movie S3 (Supporting Information), the multifunctional object successfully behaved as a magneto-electric component. Indeed, when approaching the different electrode pairs (L1-L2-L3) driven by the magnetic force generated by the external magnetic field, the object closed each electrical circuit and then activated the LED.

2.5. Antibacterial Activity of the Multifunctional Fe_3O_4-Ag Nanocomposites

At last, we tested whether the presence of Ag NPs could also impart antibacterial properties to the nanocomposites. Indeed, Ag NPs are well-known as effective biocides in many bactericidal applications due to their excellent antimicrobial upshot on drug-resistant bacteria and germicidal potency in many bacterial infections.

Nevertheless, the exact mechanism by which they exert inhibitory or bactericidal activity has not been fully elucidated yet.[90,93,94] In this regard, there is sundry evidence supporting that silver cations locally discharged from the surface of Ag NPs, due to their oxidative activity, play a pivotal role in inducing antibacterial activity via electrostatic interactions with the negatively charged membranes of bacteria.[95,96] In particular, Ag^+ ions can induce bacteria death by binding to the thiol groups found in vital enzymes on their cellular surface destroying DNA replication ability.[97–99]

Therefore, the assessment of the release of silver cations in water from the Ag NPs embedded in the $NC_{6;y*}$ samples turns out to be fundamental when foreseeing the potential application of these multifunctional nanocomposites for antibacterial purposes.

The release was measured in the different specimens after reduction, using as notation the $AgNO_3$ content in the initial formulation.

As can be observed in **Figure 5a**, the Ag^+ release shows a dose-dependent response. This is fully compatible with an ever-higher number of release sites of positively charged silver cations on the surface of the $NC_{6;y}$* samples when increasing the $AgNO_3$ dosage due to an increasing density of photogenerated Ag NPs (see EDX data in Figure 4b and FESEM images in Figure S5, Supporting Information).

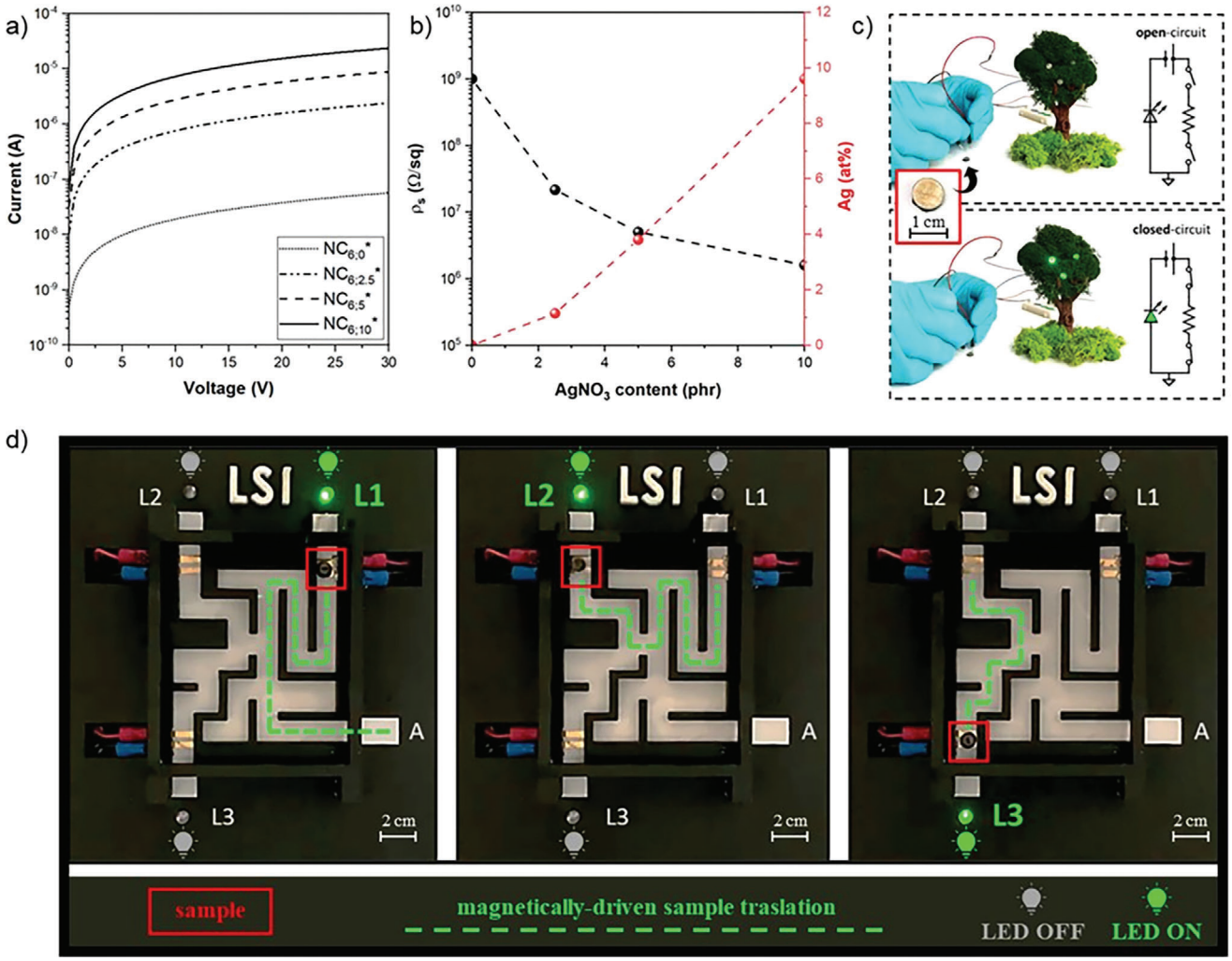

Figure 4. a) Semilogarithmic I/V plot for the $NC_{6;y}$* samples as a function of the $AgNO_3$ nanocomposite dosage; b) resistivity for the $NC_{6;y}$* samples as a function of the surface Ag content measured by EDX; c) $NC_{6;10}$* samples used as resistive component of an electric circuit: the current flowing through the object was sufficient to achieve the illumination of a led (30 Volt); d) example of the magneto-electric multifunctionality of a $NC_{6;10}$* sample which is driven into a labyrinth by the application of an external magnetic field, to close three electrical circuits and then activating the LEDs lighting.

Five strains including *Escherichia coli* K12 (MG1655), *Salmonella enterica (serovar thyphimurium*, St), *Pseudomonas aeruginosa* (PA01) and two isolates of *Staphylococcus aureus*, HG001 and the invasive USA300, were then selected to evaluate the antibacterial activity of the nanocomposites by agar disc diffusion method, i.e., by measuring the diameter of the zone of clearance around the samples, termed as zone of inhibition (ZOI), after 24 h incubation. The nanocomposite unfilled with $AgNO_3$, $NC_{6;0}$*, was used as the negative control.

E. coli was first employed to study the inhibitor activity of the $NC_{6;y}$* samples as a function of the $AgNO_3$ dosage. As shown in Figure 5b, the ZOI displayed a silver dose-dependent trend, reaching a plateau at ≈12 mm for the content of Ag NPs precursor of 2.5 phr. Noteworthy, the steeper slope of the ZOI curve was observed in the range between 0.01 and 1–2.5 phr of Ag NPs precursor, suggesting that any additional increase in its concentration would not induce a greater antibacterial effect. This was further confirmed by bacterial viability assay, as bacterial death was observed to be almost complete (92%) already for an $AgNO_3$ dosage of 1 phr (Figure 5c; Figure S6, Supporting Information).

Additional tests were then performed to evaluate the antibacterial activity of the $NC_{6;y}$* nanocomposites against different Gram-negative and Gram-positive bacteria. A new set of experiments was performed on samples loaded with only 2.5 phr of $AgNO_3$ based on the preliminary measurements with *E. coli* (see Figure 5b).

The results confirmed the excellent antibacterial activity of the magnetic $NC_{x;y}$* nanocomposites against a range of selected pathogenic bacterial strains (Figure 5d; Figure S7, Supporting Information). Between the tested bacteria, *P. aeruginosa* (PA01) has the largest ZOI of 16 mm, *S. thyphimurium* (St) the smallest (ZOI = 11 mm), while the two isolate strains of *S. aureus*, namely HG001, and USA300, have a ZOI of 12 and 13.5 mm, respectively. The differences observed in the ZOI diameter can be attributed to the different susceptibility of the various bacteria strains to the $NC_{x;y}$* nanocomposite.

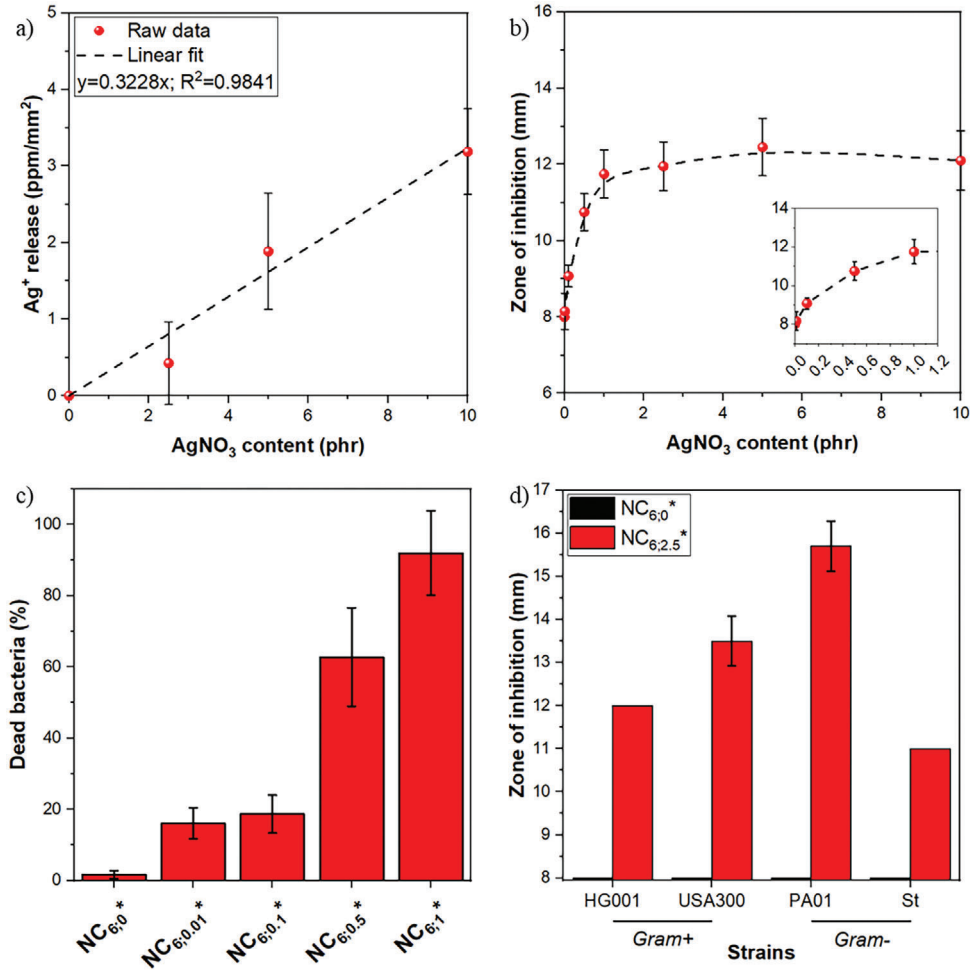

Figure 5. a) Release of silver cations from the $NC_{6;y}$* samples as a function of the $AgNO_3$ nanocomposite dosage; b) zone of inhibition of the $NC_{6;y}$* samples against *E. coli* as a function of the $AgNO_3$ dosage; c) quantification of *E. coli* mortality; d) comparative zone of inhibition of $NC_{6;2.5}$* samples having the same $AgNO_3$ dosage (2.5 phr) measured after incubation of the bacterial strains (*S. aureus* HG001 and USA300, *P. aeruginosa* PAO1 and *Salmonella typhimurium* (St) ($NC_{6;0}$*, i.e., nanocomposite sample, 8 mm diameter, unfilled with $AgNO_3$ was taken as negative control).

On the basis of these results, it is possible to envisage the potential use of these multifunctional NCs for the fabrication of dynamic devices whose antibacterial action can be locally enhanced by exploiting a magnetically driven locomotion, as demonstrated in a proof-of-concept experiment in which multifunctional nanocomposites are used as a magnetic-driven antibacterial device for biofilm eradication.

Biofilms, which are bacterial communities surrounded by a matrix of extracellular polymeric materials (e.g., exopolysaccharides), protect bacteria by acting as a barrier to antibacterial drugs.[100–102] Therefore, effective biofilm eradication turns out to be fundamental to preventing persistent infections. In this context, novel strategies have been reported to target-kill-degrade-and-remove the biofilm structure to prevent its ability to re-establish, hence acting as a reservoir of nutrients that facilitate the re-growth of bacteria.[103]

Following this approach, we tested the capability of multifunctional Fe_3O_4-Ag NCs to eradicate an *S. aureus* forming biofilm, exploiting i) Ag NPs to kill biofilm-embedded bacteria, and ii) the magnetic actuation of the NCs to physically remove the biofilm. The results, reported in SI (see Figure S8a–d, Supporting Information), show both an effective magnetically-driven mechanical destruction of the biofilm structure, in good agreement with previously reported studies[103] and, as expected, increasing killing ability of bacteria increasing the amount of silver precursors. Those findings, although preliminary, show promising ability for gathering mechanical and chemical biofilm eradication. In this sense, the ability to locally control the bactericidal action by applying a magnetic field can allow biofilm disruption in difficult-to-access locations such as catheters or implants, and its application will be the core of future investigations.

3. Conclusion

This work explores a strategy to enable multifunctionalities in 3DP processes that exploits the integration of two functional nanofillers into a polymeric resin, enabling the fabrication of 4D printable composites, and extending the definition of this class of materials given by Prof. Skylar Tibbits.

A photocurable diacrylate oligomer was loaded with both Fe_3O_4 NPs and $AgNO_3$, as a precursor for the in situ photoinduced generation of Ag NPs. The so-produced formulations were suitable for 3DP, by means of digital light processing, of multifunctional magnetic nanocomposite with integrated electrical and antibacterial functions. The presented results enlighten that adjusting the composition of the photocurable formulations leads to easily tailoring the properties of the printed samples. In particular, the magnetic response of the nanocomposites was tuned by changing the loading Fe_3O_4 NPs. This enabled the printing of structures that can be remotely controlled by the application of a localized magnetic field. Moreover, the electrical conductivity and antibacterial activity were enabled by optimizing the content of Ag NPs generated after the printing stage under UV irradiation. Indeed, increasing the $AgNO_3$ content in the printable formulations led an increased number of generated Ag NPs and hence to a reduction of the electrical resistance of the printed nanocomposites and a simultaneous increase of their antibacterial activity, as proved in different proof-of-concept experiments.

Based on these results, it is possible to foresee the application of these multifunctional nanocomposites for fabricating magneto-driven devices, as witnessed by proof-of-concept experiments here showed, which may find further development both in soft electronics and in biomedical fields.

Furthermore, such a type of multiscale approach, which exploits the integration of functional nanofillers into 3D printable polymeric matrices, may ultimately unlock unforeseen opportunities in the development of advanced and versatile 4D printed devices that can easily adapt to different application scenarios.

4. Experimental Section

Materials: Polyethylene glycol diacrylate (PEGDA, molecular weight of 700 g mol^{-1}) was used as a photocurable oligomer. Silver nitrate ($AgNO_3$) was employed as a precursor of Ag NPs while spherical-shaped iron oxide (Fe_3O_4) nanoparticles (NPs) with a nominal diameter ranging between 50 and 100 nm (98% purity) were selected as magneto-responsive nanofiller. Bis(2,4,6-trimethylbenzoyl) phenylphosphine oxide (BAPO) was chosen as a photoinitiator for its absorbance in the deep blue to near UV and 2-hydroxy-2-methyl-1-phenyl-propan-1-one (HMP) was employed as UV-photoactive compound to support the photoreduction of $AgNO_3$. All the chemicals were purchased from Sigma–Aldrich and used as received without further purification.

Preparation and Characterization of the Photocurable Formulations: The formulations were prepared by adding to PEGDA different amounts of $AgNO_3$ and Fe_3O_4 NPs, while the content of BAPO and HMP was set to 1 and 2 phr (per hundred resin), respectively, according to previous investigations.[62]

Rheological measurements were performed at a constant temperature (25 °C) using an Anton Paar Modular Compact Rheometer (Physica MCR 302) in parallel-plate mode (25 mm diameter), setting the gap between the plates to 0.2 mm and the shear frequency to 10 rad s^{-1}, while the shear rate was varied from 0.1 to 100 s^{-1}.

The same instrument was also used for real-time photorheology measurements. In this case, the rheometer was equipped with a Hamamatsu LC8 lamp (visible bulb with cut-off filter below 400 nm, equipped with 8 mm light guide, 10 mW cm^{-2}) positioned underneath the bottom plate. The gap between the plates was set to 0.2 mm and the samples were kept in isothermal condition (25 °C) and under a constant shear angular frequency (10 rad s^{-1}). The measurements were carried out in the linear viscoelastic region of the liquid formulations setting a strain amplitude of 1%. The light was switched on after 30 s to let the system stabilize before the onset of photopolymerization. The reactivity of the photocurable formulations was investigated by recording the evolution of the storage modulus of the material (G′) during the visible light irradiation and the onset of photopolymerization (i.e., the delay time required to induce crosslinking). The measurements were repeated three times for each formulation and the results were averaged.

3D Printing: The formulations were 3D-printed using a RobotFactory HD 2.0 DLP printer (nominal resolution of 50 µm in the x–y plane, while the maximum resolution in z-direction was 10 µm) equipped with a broadband projector emitting in the visible range (10 mW cm^{-2}).

The exposure time was set at 1.5 s per layer for the formulations containing the lowest content of Fe_3O_4, and increased up to 3 s per layer for 6 phr of Fe_3O_4, while the layer thickness was set at 25 µm. In order to improve the adhesion of the printed structures to the building platform, a base layer depleted of Fe_3O_4 NPs was fabricated before the printing of the final object. In this case, the exposure time for neat PEGDA was set at 1 s per layer.

UV Postprocessing: A medium-pressure mercury Hamamatsu LC8 UV lamp equipped with an 8 mm light guide was used to perform the UV postprocessing (10 min irradiation, light intensity of ≈100 mW cm^{-2}, measured with an EIT radiometer).

Characterization of the Multifunctional Fe_3O_4–Ag Nanocomposites: 3D scanning was performed with a 3D optical scanner (E3, 3Shape), to evaluate the fidelity of the built objects to the original CAD models. The scanned data and the reference model were aligned before being compared. The results of the comparative analysis were displayed as a heatmap showing the geometrical deviation from the reference model.

Morphological characterization of the nanocomposites was carried out by field emission scanning electron microscopy (FESEM), using a FEI Quanta 600 FESEM equipped with an EDX for compositional analyses. The images were taken in high vacuum mode and 10 KeV voltage.

UV–vis spectroscopy measurements were performed using a UV-2600i spectrophotometer (Shimadzu), equipped with an integrating sphere, in reflectance mode. Diffuse spectra were recorded between 190 and 900 nm with a medium scan speed and setting a scan step of 0.5 nm. The results were analyzed using LabSolutions UV–vis dedicated software.

Room-temperature hysteresis loops were measured by means of a vibrating sample magnetometer (Lakeshore 7400). The samples (3 × 3 × 3 mm) were mounted on a quartz sample-holder rod and submitted to a magnetic field (H) ranging in the interval −15 kOe < H < 15 kOe. The magnetometer is routinely calibrated by means of a standard nickel sphere and the spurious diamagnetic signal from the sample-holder was duly considered and accurately subtracted. The results were averaged over three measurements.

The x–y displacements of the magnetic elements were controlled using a custom-made system based on CoreXY displacement principle with two stepper motors in micro-stepper configuration and GRBL open-source g-code (https://github.com/grbl/grbl) installed on an Arduino Mega microcontroller (Figure S9, Supporting Information).

A PHI 5000 Versaprobe scanning X-ray photoelectron spectrometer (monochromatic Al Kα X-ray source with 1486.6 eV energy, 15 kV voltage, and 1 mA anode current) was used to investigate the distribution of Ag NPs in the postprinting UV-irradiated nanocomposites. A spot size of 100 µm was used to collect the photoelectron signal for both the high-resolution (HR) and the survey spectra. Different pass energy values were exploited: 187.8 eV for survey spectra and 23.5 eV for HR peaks. All samples were analyzed with a combined electron and Ar ion gun neutralizer system to reduce the charging effect during the measurements. All core-level peak energies were referred to C 1s peak at 284.5 eV, and the background contribution, in HR scans, was subtracted by means of a Shirley function. Spectra were analyzed using Multipak 9.6 dedicated software. Depth profiles were performed in an alternate mode with sputtering cycles of 1 min each (Ar^+ flux at 2 kV accelerating voltage).

Electrical measurements were performed using a Keithley 4200A-SCS Voltage Source Measure Unit, by contacting tungsten microneedles on a two-point contact setup realized by placing silver paste on the edges of the samples (5 × 5 × 1 mm) The tests were carried out setting a voltage

linear sweep (voltage range ±30 V), a scan step of 0.5 V and a compliance of 70 mA. The curves reported an average 3 I–V cycles.

The Ag^+ released from the nanocomposites was measured by an in situ colorimetric assay, using 3,3′,5,5′-tetramethylbenzidine (TMB) as a selective indicator.[104,105] Briefly, the addition of TMB and an acetate buffer solution (NaAc/AcH) to an aqueous colorless solution containing Ag^+ released from the $NC_{x;y}$* samples give rise to the oxidized form of TMB (oxTMB) and Ag(0), a blue color in aqueous solution. The reaction can be monitored by absorption spectroscopy, following the typical peak of oxTMB at 650 nm. In a typical run, the sample surface was incubated with 20 µL of dH_2O in a wet chamber at 22 °C for 30 min, then the amount was collected from each sample, separately. For each sample, a master mixture was prepared (total volume 250 µL), as follows: buffer NaAc/AcH (pH 4) 33.3 µL, TMB solution 0.66 mM 16.7 µL, sample Ag^+ 20 µL and dH_2O 180 µL. The master mixture was incubated at RT for 15 min (starting when the sample Ag^+ was added) and analyzed by means of UV–vis spectra at room temperature. The difference between absorbance at 650 nm and 540 (baseline) was calculated and used to determine sample concentration according to the calibration curve for Ag^+. The results were normalized to the sample surface area and averaged over multiple measurements.

Five strains *Escherichia coli* K12 (MG1655), *Salmonella enterica (serovar typhimurium*, St) and *Pseudomonas aeruginosa* (PA01) strains, and two isolates of Gram-positive *Staphylococcus aureus* strain, HG001, and the invasive USA300, were then selected to evaluate the antibacterial activity of the nanocomposites by agar disc diffusion method, i.e., by measuring the zone of clearance around the samples, termed as the zone of inhibition (ZOI), after 24 h incubation. Precultures were first grown overnight (O/N) in Luria-Bertani (LB) or Mueller Hinton Broth (MHB), diluted, and finally grown in the same media until an optical density OD_{600} of 0.8-1 (exponential phase). Finally, 100 µL was uniformly spread on LB or MHB plates. The nanocomposite samples (8 mm diameter) were sterilized under UV light for 30 min and then deposited on the plates before O/N incubation at 37 °C. The ZOI is obtained by measuring the diameter (in mm) of the zone of clearance around the circular sample. The obtained ZOI value is inversely proportional to the resistance of the bacteria tested.[106]

The bacterial viability in solution was quantified by using the standard staining microscopy method LIVE/DEAD BacLightTM kit (Thermofisher, Waltham, MA, USA), which allows the direct differentiation between total and dead bacteria using two fluorescent probes: Syto 9, which stains total bacteria as it penetrates living and dead cells; and propidium iodide, which selectively penetrates dead bacteria with damaged membrane. Staining was performed according to the manufacturer's protocol. The bacterial viability was evaluated after O/N incubation with the DLP printed and UV postprocessed samples. The results were averaged over multiple measurements.

Biofilm eradication tests were performed as follows. Precultures of *S. aureus* HG001 were grown overnight in BHI medium (Difco). The culture was diluted to OD_{600} = 0.05 and seeded in two 6-well plates. DLP-printed $NC_{x;y}$* samples containing different concentrations of $AgNO_3$ (0, 2,5%, 5%, and 10%) were placed in the center of the plates, which were incubated at 37 °C without shaking. After 6 h of incubation, supernatants containing planktonic bacteria were removed and their OD_{600} was measured. The adherent bacteria were either stained by crystal violet 0.1% after removing the $NC_{x;y}$* samples or 2 mL of BHI was added to detach mechanically the bacteria. Biofilms were disrupted by moving the $NC_{x;y}$* samples with a magnet and the OD_{600} of the suspension was measured and serially diluted on plates for viability counting.

Supporting Information

Supporting Information is available from the Wiley Online Library or from the author.

Acknowledgements

This work was funded by the Commissariat à l'Energie Atomique et aux Energies Alternatives (CEA) through the project Quattro-D of the Program Transversal de Compétences (PTC). This work was supported by a public grant overseen by the French National Research Agency (ANR) as part of the « Investissements d'Avenir » program, through the "ADI 2021" project funded by the IDEX Paris-Saclay, ANR-11-IDEX-0003-02 (FT). This work was supported by the National Plan for Complementary Investments to the NRRP, project "D34H—Digital Driven Diagnostics, prognostics and therapeutics for sustainable Health care" (project code: PNC0000001), Spoke 4 funded by the Italian Ministry of University and Research. This research benefited, through the use of PLATINE platform, from the support of the Ecole Polytechnique fundraising–Smart Environments: Nanosensors and Nanoreliability Initiative. The authors thank Hugo Chauvet (Synchrotron SOLEIL), for his initial support in fluorescence measurements, and Dr. Federica Banche Niclot and Dr. Mattia Pagani for their help in the Ag^+ release investigations.

Conflict of Interest

The authors declare no conflict of interest.

Data Availability Statement

The data that support the findings of this study are available in the supplementary material of this article.

Keywords

4D printing, multifunctional nanocomposites, nanoparticles, smart device

Received: April 12, 2024
Revised: July 2, 2024
Published online: July 11, 2024

[1] I. Gibson, D. Rosen, B. Stucker, M. Khorasani, *Additive Manufacturing Technologies*, Springer International Publishing, Cham **2021**.
[2] S. A. Kumar, R. V. S. Prasad, in *Additive Manufacturing: A Tool for Industrial Revolution 4.0*, (Eds: M. Manjaiah, K. Raghavendra, N. Balashanmugam, J. Paulo Davim), Elsevier- Woodhead Publishing, United Kingdom **2021**, Ch. 2.
[3] B. Sandeep, T. T. M. Kannan, J. Chandradass, M. Ganesan, A. John Rajan, *Mater. Today Proc* **2021**, *45*, 6941.
[4] R. Kumar, M. Kumar, J. S. Chohan, *Bull. Mater. Sci.* **2021**, *443*, 181.
[5] F. Matos, R. Godina, C. Jacinto, H. Carvalho, I. Ribeiro, P. Peças, *Sustainbility* **2019**, *11*, 3757.
[6] G. Gonzalez, I. Roppolo, C. F. Pirri, A. Chiappone, *Addit. Manuf.* **2022**, *55*, 102867.
[7] T. A. Campbell, S. Tibbits, B. Garrett, *Sci. Am. Magazine* **2014**, *311*, 60.
[8] R. Bogue, *Assem. Autom.* **2014**, *34*, 16.
[9] S. Das, T. L. Alford, *JOM* **2013**, *65*, 538.
[10] S. Bahl, H. Nagar, I. Singh, S. Sehgal, *Mater. Today Proc.* **2020**, *28*, 1302.
[11] M. Su, Y. Song, *Chem. Rev.* **2022**, *122*, 5144.
[12] F. Soto, E. Karshalev, F. Zhang, B. Esteban Fernandez de Avila, A. Nourhani, J. Wang, *Chem. Rev.* **2022**, *122*, 5365.
[13] S. Tibbits, *Archit. Des.* **2014**, *84*, 116.
[14] S. Joshi, K. Rawat, Karunakaran C, V. Rajamohan, A. T. Mathew, K. Koziol, V. Kumar Thakur, Balan A. S. S, *Appl. Mater. Today* **2020**, *18*, 100490.
[15] A. Mitchell, U. Lafont, M. Hołyńska, C. Semprimoschnig, *Addit. Manuf.* **2018**, *24*, 606.

[16] X. Kuang, D. J. Roach, J. Wu, C. M. Hamel, Z. Ding, T. Wang, M. L. Dunn, H. J. Qi, *Adv. Funct. Mater.* **2019**, *29*, 1805290.
[17] M. Rafiee, R. D. Farahani, D. Therriault, *Adv. Sci.* **2020**, *7*, 1902307.
[18] L. R. Lopes, A. F. Silva, O. S. Carneiro, *Addit. Manuf.* **2018**, *23*, 45.
[19] A. Bandyopadhyay, B. Heer, *Mater. Sci. Eng. R Rep.* **2018**, *129*, 1.
[20] Y. L. Kong, *Nature* **2023**, *623*, 488.
[21] K. Benyahia, H. Seriket, R. Prod'hon, S. Gomes, J. C. André, H. J. Qi, F. Demoly, *Proc. CIRP* **2023**, *119*, 396.
[22] D. G. Bekas, Y. Hou, Y. Liu, A. Panesar, *Compos. Part B Eng.* **2019**, *179*, 107540.
[23] R. G. Burela, J. N. Kamineni, D. Harursampath, in *3D and 4D Printing of Polymer Nanocomposites Materials: Processing, Applications and Challenges* (Eds.: K.K. Sadasivuni, K. Deshmukh, M.A. Almaadeed), Elsevier, The Netherlands **2020**, Ch. 8.
[24] M. Falahati, P. Ahmadvand, S. Safaee, Y. C. Chang, Z. Lyu, R. Chen, L. Li, Y. Lin, *Mater. Today* **2020**, *40*, 215.
[25] A. Cortés, A. Cosola, M. Sangermano, M. Campo, S. González Prolongo, C. F. Pirri, A. Jiménez-Suárez, A. Chiappone, *Adv. Funct. Mater.* **2021**, *31*, 2106774.
[26] P. Galliker, J. Schneider, H. Eghlidi, S. Kress, V. Sandoghdar, D. Poulikakos, *Nat. Commun.* **2012**, *3*, 890.
[27] S. Z. Guo, X. Yang, M. C. Heuzey, D. Therriault, *Nanoscale* **2015**, *7*, 6451.
[28] C. Reyes, R. Somogyi, S. Niu, M. A. Cruz, F. Yang, M. J. Catenacci, C. P. Rhodes, B. J. Wiley, *ACS Appl. Energy Mater.* **2018**, *1*, 5268.
[29] Y. Wang, C. Chen, H. Xie, T. Gao, Y. Yao, G. Pastel, X. Han, Y. Li, J. Zhao, K. Fu, L. Hu, Y. Wang, J. Zhao, C. Chen, H. Xie, T. Gao, Y. Yao, G. Pastel, X. Han, Y. Li, K. Fu, L. Hu, *Adv. Funct. Mater.* **2017**, *27*, 1703140.
[30] J. J. Adams, E. B. Duoss, T. F. Malkowski, M. J. Motala, B. Yeop Ahn, R. G. Nuzzo, J. T. Bernhard, J. A. Lewis, J. J. Adams, J. T. Bernhard, E. B. Duoss, T. F. Malkowski, B. Y. Ahn, J. A. Lewis, M. J. Motala, R. G. Nuzzo, *Adv. Mater.* **2011**, *23*, 1335.
[31] G. Postiglione, G. Natale, G. Griffini, M. Levi, S. Turri, *Compos. Part A Appl. Sci. Manuf.* **2015**, *76*, 110.
[32] Q. Guo, R. Ghadiri, S. Xiao, C. Esen, O. Medenbach, A. Ostendorf, *SPIE* **2012**, *8243*, 24.
[33] H. Kim, T. Fernando, M. Li, Y. Lin, T. L. B. Tseng, *J. Compos. Mater.* **2018**, *52*, 197.
[34] R. D. Farahani, H. Dalir, V. L. Borgne, L. A. Gautier, M. A. El Khakani, M. Lévesque, D. Therriault, *Nanotechnology* **2012**, *23*, 085502.
[35] S. J. Leigh, C. P. Purssell, J. Bowen, D. A. Hutchins, J. A. Covington, D. R. Billson, *Sens. Act. A Phys.* **2011**, *168*, 66.
[36] N. J. Castro, R. Patel, L. G. Zhang, *Cell. Mol. Bioeng.* **2015**, *8*, 416.
[37] S. Ahmadi, P. Nassiri, I. Ghasemi, M. R. Monazzam Ep, *Glob. J. Health Sci.* **2015**, *8*, 180.
[38] J. J. Martin, B. E. Fiore, R. M. Erb, *Nat. Commun.* **2015**, *6*, 8641.
[39] H. W. Huang, M. S. Sakar, A. J. Petruska, S. Pané, B. J. Nelson, *Nat. Commun.* **2016**, *7*, 12263.
[40] T. Hu, S. Xuan, L. Ding, X. Gong, *Mater. Des.* **2018**, *156*, 528.
[41] G. Yun, S. Y. Tang, S. Sun, D. Yuan, Q. Zhao, L. Deng, S. Yan, H. Du, M. D. Dickey, W. Li, *Nat. Commun.* **2019**, *10*, 1300.
[42] M. Xie, W. Zhang, C. Fan, C. Wu, Q. Feng, J. Wu, Y. Li, R. Gao, Z. Li, Q. Wang, Y. Cheng, B. He, M. Xie, Q. Feng, J. Wu, Y. Li, R. Gao, Z. Li, Y. Cheng, W. Zhang, C. Fan, B. He, C. Wu, Q. Wang, *Adv. Mater.* **2020**, *32*, 2000366.
[43] A. Cortés, J. L. Aguilar, A. Cosola, X. X. Fernández Sanchez-Romate, A. Jiménez-Suárez, M. Sangermano, M. Campo, S. G. Prolongo, *ACS Appl. Polym. Mater.* **2021**, *3*, 5207.
[44] L. Zhang, X. Zhang, L. Li, Y. Liu, D. Wang, L. Xu, J. Bao, A. Zhang, L. Zhang, X. Zhang, Y. Liu, D. Wang, L. Xu, J. Bao, A. Zhang, *Macromol. Mater. Eng.* **2020**, *305*, 1900718.
[45] Y. Luo, X. Wei, Y. Wan, X. Lin, Z. Wang, P. Huang, *Acta Biomater.* **2019**, *92*, 37.
[46] T. J. Wallin, J. Pikul, R. F. Shepherd, *Nat. Rev. Mater.* **2018**, *3*, 84.
[47] M. Hasan, D. Ansari, V. Iacovacci, S. Pane, M. Ourak, G. Borghesan, I. Tamadon, E. Vander Poorten, A. Menciassi, M. H. D. Ansari, V. Iacovacci, S. Pane, A. Menciassi, M. Ourak, G. Borghesan, E. Vander Poorten, *Adv. Funct. Mater.* **2023**, *33*, 2211918.
[48] Z. Li, Y. P. Lai, E. Diller, *Adv. Intell. Syst.* **2024**, *6*, 2300052.
[49] R. Tognato, A. R. Armiento, V. Bonfrate, R. Levato, J. Malda, M. Alini, D. Eglin, G. Giancane, T. Serra, R. Tognato, A. R. Armiento, M. Alini, D. Eglin, T. Serra, V. Bonfrate, G. Giancane, R. Levato, J. Malda, *Adv. Funct. Mater.* **2019**, *29*, 1804647.
[50] X. Lin, M. Han, *Soft Sci.* **2023**, *3*, 14.
[51] A. Ali, T. Shah, R. Ullah, P. Zhou, M. Guo, M. Ovais, Z. Tan, Y. K. Rui, *Front. Chem.* **2021**, *9*, 629054.
[52] X. Peng, X. Kuang, D. J. Roach, Y. Wang, C. M. Hamel, C. Lu, H. J. Qi, *Addit. Manuf.* **2021**, *40*, 101911.
[53] I. J. Fernandes, A. F. Aroche, A. Schuck, P. Lamberty, C. R. Peter, W. Hasenkamp, T. L. A. C. Rocha, *Sci. Reports* **2020**, *10*, 8878.
[54] I. Bayraktar, D. Doganay, S. Coskun, C. Kaynak, G. Akca, H. E. Unalan, *Compos. Part B Eng.* **2019**, *172*, 671.
[55] Y. Hang, A. Wang, N. Wu, *Chem. Soc. Rev.* **2024**, *53*, 2932.
[56] M. Shah, A. Ullah, K. Azher, A. U. Rehman, W. Juan, N. Aktürk, C. S. Tüfekci, M. U. Salamci, *RSC Adv.* **2023**, *13*, 1456.
[57] Y. Li, W. Wang, F. Wu, R. K. Kankala, *Front. Mater.* **2023**, *9*, 1118943.
[58] S. Lantean, G. Barrera, C. F. Pirri, P. Tiberto, M. Sangermano, I. Roppolo, G. Rizza, *Adv. Mater. Technol.* **2019**, *4*, 1900505.
[59] S. Lantean, I. Roppolo, M. Sangermano, M. Hayoun, H. Dammak, G. Rizza, *Addit. Manuf.* **2021**, *47*, 102343.
[60] S. Lantean, I. Roppolo, M. Sangermano, M. Hayoun, H. Dammak, G. Barrera, P. Tiberto, C. F. Pirri, L. Bodelot, G. Rizza, *Adv. Mater. Technol.* **2022**, *7*, 2200288.
[61] E. Fantino, A. Chiappone, F. Calignano, M. Fontana, F. Pirri, I. Roppolo, *Materials* **2016**, *9*, 589.
[62] E. Fantino, A. Chiappone, I. Roppolo, D. Manfredi, R. Bongiovanni, C. F. Pirri, F. Calignano, *Adv. Mater.* **2016**, *28*, 3712.
[63] C. Zhang, X. Li, L. Jiang, D. Tang, H. Xu, P. Zhao, J. Fu, Q. Zhou, Y. Chen, *Adv. Funct. Mater.* **2021**, *31*, 2102777.
[64] X. Wei, M.-L. Jin, H. Yang, X.-X. Wang, Y.-Z. Long, Z. Chen, *J. Adv. Ceram.* **2022**, *2022*, 665.
[65] L. Sang, E. Franco-Urquiza, S. Leong Sing, G. Ehrmann, T. Blachowicz, A. Ehrmann, *Polymer* **2022**, *14*, 3895.
[66] H. Jin, H. Guo, X. Gao, R. Gui, *Sens. Act. B Chem.* **2018**, *277*, 14.
[67] E. T. Tenório-Neto, M. R. Guilherme, M. E. G. Winkler, L. Cardozo-Filho, S. C. Beneti, A. F. Rubira, M. H. Kunita, *Mater. Lett.* **2015**, *159*, 118.
[68] L. M. Valencia, M. Herrera, M. de la Mata, J. Hernández-Saz, I. Romero-Ocaña, F. J. Delgado, J. Benito, S. I. Molina, *Polymers (Basel)* **2022**, *14*, 5238.
[69] C. Sciancalepore, F. Moroni, M. Messori, F. Bondioli, *Compos. Commun.* **2017**, *6*, 11.
[70] A. J. Lopes, I. H. Lee, E. Macdonald, R. Quintana, R. Wicker, *J. Mater. Process. Technol.* **2014**, *214*, 1935.
[71] J. W. Li, H. F. Chen, Y. Z. Liu, J. H. Wang, M. C. Lu, C. W. Chiu, *Chem. Eng. J.* **2024**, *484*, 149452.
[72] Y. Xiong, F. Zhou, D. Zhu, *IOP Conf. Ser. Mater. Sci. Eng.* **2022**, *1248*, 012003.
[73] G. A. González Flores, V. Bertana, A. Chiappone, I. Roppolo, L. Scaltrito, S. L. Marasso, M. Cocuzza, G. Massaglia, M. Quaglio, C. F. Pirri, S. Ferrero, *Macromol. Mater. Eng.* **2022**, *307*, 2100596.
[74] G. Taormina, C. Sciancalepore, F. Bondioli, M. Messori, *Polymer* **2018**, *10*, 212.
[75] Z. Weng, X. Huang, S. Peng, L. Zheng, L. Wu, *Nat. Commun.* **2023**, *14*, 4303.
[76] Y. Luo, G. Le Fer, D. Dean, M. L. Becker, *Biomacromolecules* **2019**, *20*, 1699.

[77] M. Caprioli, I. Roppolo, A. Chiappone, L. Larush, C. F. Pirri, S. Magdassi, *Nat. Commun.* **2021**, *12*, 2462.
[78] I. Roppolo, A. Chiappone, A. Angelini, S. Stassi, F. Frascella, C. F. Pirri, C. Ricciardi, E. Descrovi, *Mater. Horiz.* **2017**, *4*, 396.
[79] S. Stassi, E. Fantino, R. Calmo, A. Chiappone, M. Gillono, D. Scaiola, C. F. Pirri, C. Ricciardi, A. Chiadò, I. Roppolo, *ACS Appl. Mater. Interfaces* **2017**, *9*, 19193.
[80] A. Schlegel, S. F. Alvarado, P. Wachter, *J. Phys. C Solid State Phys.* **1979**, *12*, 6.
[81] K. D. Jandt, R. W. Mills, *Dent. Mater.* **2013**, *29*, 605.
[82] A. Barbieri, G. Accorsi, N. Armaroli, *Chem. Commun.* **2008**, *21*, 2185.
[83] Y. Xia, Y. Xiong, B. Lim, S. E. Skrabalak, *Angew. Chem., Int. Ed.* **2009**, *48*, 60.
[84] I. Roppolo, M. Castellino, K. Bejtka, G. Rizza, D. Perrone, P. E. Coulon, A. Chiappone, K. Rajan, S. Bocchini, C. Ricciardi, C. F. Pirri, A. Chiolerio, *J. Phys. Chem. C* **2017**, *121*, 14285.
[85] I. Roppolo, A. Doriguzzi Bozzo, M. Castellino, A. Chiappone, D. Perrone, K. Bejtka, S. Bocchini, M. Sangermano, A. Chiolerio, *RSC Adv.* **2016**, *6*, 14832.
[86] P. Taneja, P. Ayyub, R. Chandra, *Phys. Rev. B* **2002**, *65*, 245412.
[87] M. Milošević, M. Radoičić, Z. Šaponjić, T. Nunney, C. Deeks, V. Lazić, M. Mitrić, T. Radetić, M. Radetić, *Cellulose* **2014**, *21*, 3781.
[88] A. Chiappone, M. Gillono, M. Castellino, K. Bejtka, K. Rajan, I. Roppolo, D. Perrone, S. Bocchini, C. Ricciardi, C. F. Pirri, A. Chiolerio, *Appl. Surf. Sci.* **2018**, *455*, 418.
[89] A. Bouafia, S. E. Laouini, A. S. A. Ahmed, A. V. Soldatov, H. Algarni, K. F. Chong, G. A. M. Ali, *Nanomaterials* **2021**, *11*, 2318.
[90] T. Bruna, F. Maldonado-Bravo, P. Jara, N. Caro, *Int. J. Mol. Sci.* **2021**, *22*, 7202.
[91] A. Salleh, R. Naomi, N. D. Utami, A. W. Mohammad, E. Mahmoudi, N. Mustafa, M. B. Fauzi, *Nanomaterials* **2020**, *10*, 1566.
[92] J. Hu, M. F. Yu, *Science* **2010**, *329*, 313.
[93] E. D. Cavassin, L. F. P. de Figueiredo, J. P. Otoch, M. M. Seckler, R. A. de Oliveira, F. F. Franco, V. S. Marangoni, V. Zucolotto, A. S. S. Levin, S. F. Costa, *J. Nanobiotechnology* **2015**, *13*, 64.
[94] N. Tripathi, M. K. Goshisht, *ACS Appl. Bio Mater.* **2022**, *5*, 1391.
[95] Z. M. Xiu, Q. B. Zhang, H. L. Puppala, V. L. Colvin, P. J. J. Alvarez, *Nano Lett.* **2012**, *12*, 4271.
[96] A. Kędziora, R. Wieczorek, M. Speruda, I. Matolínová, T. M. Goszczyński, I. Litwin, V. Matolín, G. Bugla-Płoskońska, *Front. Microbiol.* **2021**, *12*, 659614.
[97] P. Madhavan, P. Y. Hong, R. Sougrat, S. P. Nunes, *ACS Appl. Mater. Interfaces* **2014**, *6*, 18497.
[98] M. R. Bindhu, M. Umadevi, *Spectrochim. Acta Part A Mol. Biomol. Spectrosc.* **2015**, *135*, 373.
[99] A. J. Sorinolu, V. Godakhindi, P. Siano, J. L. Vivero-Escoto, M. Munir, *Mater. Adv.* **2022**, *3*, 9090.
[100] H. C. Flemming, J. Wingender, U. Szewzyk, P. Steinberg, S. A. Rice, S. Kjelleberg, *Nat. Rev. Microbiol.* **2016**, *14*, 563.
[101] H. Koo, R. N. Allan, R. P. Howlin, P. Stoodley, L. Hall-Stoodley, *Nat. Rev. Microbiol.* **2017**, *15*, 740.
[102] B. W. Peterson, Y. He, Y. Ren, A. Zerdoum, M. R. Libera, P. K. Sharma, A. J. van Winkelhoff, D. Neut, P. Stoodley, H. C. van der Mei, H. J. Busscher, *FEMS Microbiol. Rev.* **2015**, *39*, 234.
[103] G. Hwang, A. J. Paula, E. E. Hunter, Y. Liu, A. Babeer, B. Karabucak, K. Stebe, V. Kumar, E. Steager, H. Koo, *Sci. Robot.* **2019**, *4*, 2388.
[104] S. Liu, J. Tian, L. Wang, X. Sun, *Sens. Act. B Chem.* **2012**, *165*, 44.
[105] R. A. González-Fuenzalida, Y. Moliner-Martínez, M. González-Béjar, C. Molins-Legua, J. Verdú-Andres, J. Pérez-Prieto, P. Campins-Falcó, *Anal. Chem.* **2013**, *85*, 10013.
[106] M. Balouiri, M. Sadiki, S. K. Ibnsouda, *J. Pharm. Anal.* **2016**, *6*, 71.